J. Fluid Mech. (2016), *vol.* 792, *pp.* 658–681. © Cambridge University Press 2016
doi:10.1017/jfm.2016.97

The dynamics of dense particle clouds subjected to shock waves. Part 1. Experiments and scaling laws

Theo G. Theofanous[1,†], Vladimir Mitkin[2] and Chih-Hao Chang[3]

[1]Chemical Engineering Department, University of California, Santa Barbara, CA 93106, USA

[2]Aerospace Research Laboratory, University of Virginia, Charlottesville, VA 22904, USA

[3]Theofanous Co. Inc., Santa Barbara, CA 93109, USA

(Received 10 March 2015; revised 31 January 2016; accepted 2 February 2016;
first published online 3 March 2016)

We quantify experimentally the dispersal characteristics of dense particle clouds in high-speed interactions with an atmosphere. Focused on the fundamentals, the experiments, conducted in a large-scale shock tube, involve a well-characterized 'curtain' of (falling) particles that fully occupies the cross-sectional area of the expansion section. The particle material (glass) and size (∼1 mm) are fixed, as is the curtain thickness (∼30 mm) and the particle volume fractions in it, varying from ∼58 % at the top of the curtain to ∼24 % near the bottom. Thus, the principal experimental variable is the impacting shock strength, with Mach numbers varying from 1.2 to 2.6, and flow speeds that cover from subsonic ($M_{IS} \sim 0.3$) to transonic and supersonic ($M_{IS} \sim 1.2$). The peak shock pressure ratio, 7.6, yields a flow speed of ∼630 m s^{-1}, and a curtain expansion rate at ∼20 000 g. We record visually (high-speed, particle-resolving shadowgraphic method) the reflected/transmitted pressure waves and the transmitted contact wave, as well as the curtain displacements, and we measure the reflected/transmitted pressure transients. Data analysis yields simple rules for the amplitudes of the reflected pressure waves and the rapid cloud expansions observed, and we discover a time scaling that hints at a universal regime for cloud expansion. The data and these data-analysis results can provide the validation basis for numerical simulations meant to enable a deeper understanding of the key physics that drive this rather complex dispersal process.

Key words: particle/fluid flow, multiphase flow, shock waves

1. Introduction

This paper is concerned with the response of finite-dimension, heavy-particle clouds interacting with a high-speed, compressible, gaseous atmosphere, as found for example in the blast behind a shock wave. In a simple, curtain-like cloud geometry we have a canonical problem with all key features of highly non-equilibrium disperse multiphase flows participating interactively to produce the dispersals observed in practice. With dilute clouds the dispersals are mild and mainly due to particle-size fractionation

† Email address for correspondence: theo@theofanous.net

(Chang *et al.* 2011) and, on the longer term, due to turbulent dispersion. With dense clouds, pressure gradients, and consequently also velocity and density gradients, can be significant, inducing differential accelerations and thus cloud dimensional changes. These changes can be rather significant, as demonstrated recently (Wagner *et al.* 2012), and they provide a sensitive measure of the aforementioned interactions (Ling *et al.* 2012). More detailed, albeit significantly simplified, numerical simulations, attempting to resolve individual particles, suggest a still higher level of complexity yet to be understood (Regele *et al.* 2014). A recent extensive review (Subramaniam 2013) provides further perspectives on the magnitude of the problems in the broader area of disperse multiphase flows and theoretical/numerical approaches to them. Besides its clear fundamental interest, the problem is of central significance in the design of advanced combustion systems, and in assessing the performance of heterogeneous explosives, explosion-mitigation measures and atmospheric dissemination of liquid or dusty agents. The latter is the area of application that motivates the present work (Babarsky & Theofanous 2010).

The goal of the work presented herein is to provide a basis for understanding the above-described multiphase interactions, as a crucial part of a much broader program addressing the above-stated application (Chang *et al.* 2011). The other thrust extends from the fundamental aspects of fragmentation at the local (droplet) scale (Theofanous 2011; Theofanous *et al.* 2012; Chang, Deng & Theofanous 2013; Theofanous, Mitkin & Ng 2013), to the integral representation of a dissemination event (Theofanous *et al.* 2006). All of these efforts are supported by the experimental facility ASOS, a shock tube designed and built at the Center for Risk Studies and Safety (CRSS, UCSB) with these diverse duties in mind. Specifically, we required a large enough cross-sectional area to accommodate scaling studies on liquid and/or particulate masses involved, and a long, transparent test section, allowing observation of the fragmenting and/or dispersing clouds through their approach to equilibrium. A large catch tank is also provided to dissipate the blast and eliminate upstream-reflected shock waves. This catch tank also allows for blast-impacts research in free field, collection of debris material when needed, and it is filtered-vented for tests involving materials that need to be contained.

The ASOS experiments presented here are intended to extend those of Wagner *et al.* (2012), aiming principally to provide a broad coverage of flow conditions, spanning from subsonic, to transonic and supersonic, and much larger curtain dimensions. Moreover, we record cloud expansions comprehensively, covering from the early, highly dynamic interactions well into the long term, as the clouds approach the dilute stage. In this way, we are able to distinguish significant systematic trends, define the principal interaction regimes, and thereby provide clues about the key physics over the entire history of dispersal. On the other hand, these results provide a definitive set of validation cases for numerical simulations; thus opening the way for the in-depth analyses needed to sort out the role of the various contributions to the integrated experimental results, and ultimately to predictions in complex practical settings.

The experiments are focused on a ‘full’ curtain; that is, occupying completely the cross-sectional area of the flow channel. As compared with the partial (87 %) coverage employed by Wagner, this eliminates regions of flow bypass (and associated particle entrainment) as well as complex 3D effects on the pressure-wave dynamics. However, still some 3D complexity due to wall boundary layers at the curtain edges remains. Other differences from this previous work are: (1) particle size and curtain thickness, both scaled up by an order of magnitude (as is the Reynolds number range), and (2) visualizations resolving particles in the full-curtain field of view. In this way individual

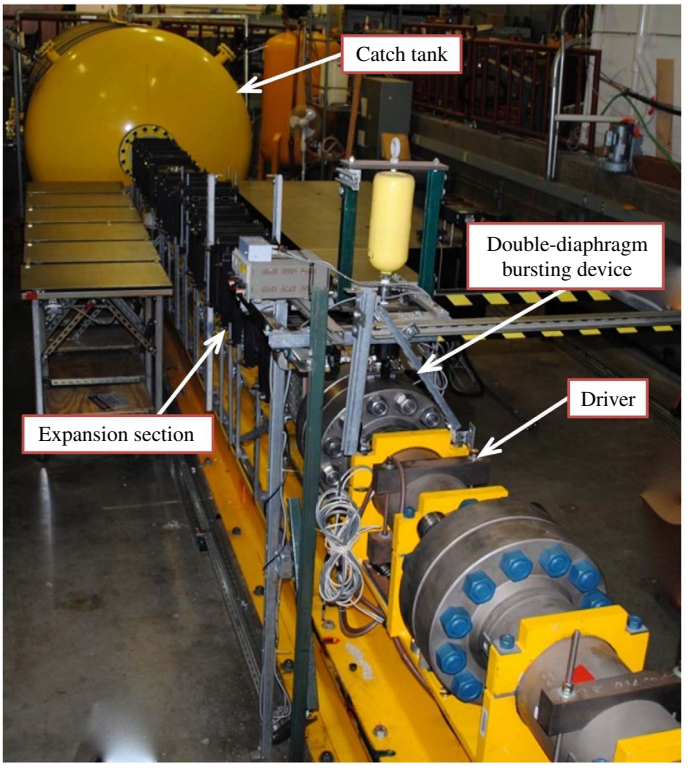

FIGURE 1. (Colour online) An overall view of the ASOS shock tube with identification of the key components. During operation, the test section and the optical tables carrying the lasers, optics and high-speed (and higher-resolution single-frame) recording instrumentation, are isolated from the surroundings by laser-safety-grade fabric 'walls'.

particle motions can be examined both at the upstream and the downstream fronts (UF, DF, respectively), as well as in significant portions of the whole clouds when they reach a dilute stage (volume fractions less than $\sim 2\,\%$).

2. The experiment set-up

The principal components of the ASOS shock tube, driver, double-diaphragm bursting device and expansion section, can be seen in the overall perspective of figure 1, and with dimensions in the schematic of figure 2. The expansion section consists of a short transition piece, taking the flow smoothly from the circular cross-section of the driver to the square one, 200×200 mm^2, of the development section, and the test section proper, which connects to the catch tank. All of these components are long enough to yield the design objective of steady blast duration as described below. Polycarbonate construction of the test section allows for nearly uninhibited visual access. The structural design envelope is defined by the release of 10 MPa Helium in the driver: it yields Mach 3.6 shocks and gas-dynamic pressures of 1.5 MPa. In the present experiments we are limited by the strong reflection from the curtain to 4 MPa Helium in the driver. The double-diaphragm bursting device, equipped with home-made diaphragms from Mylar stock, allows on-demand release

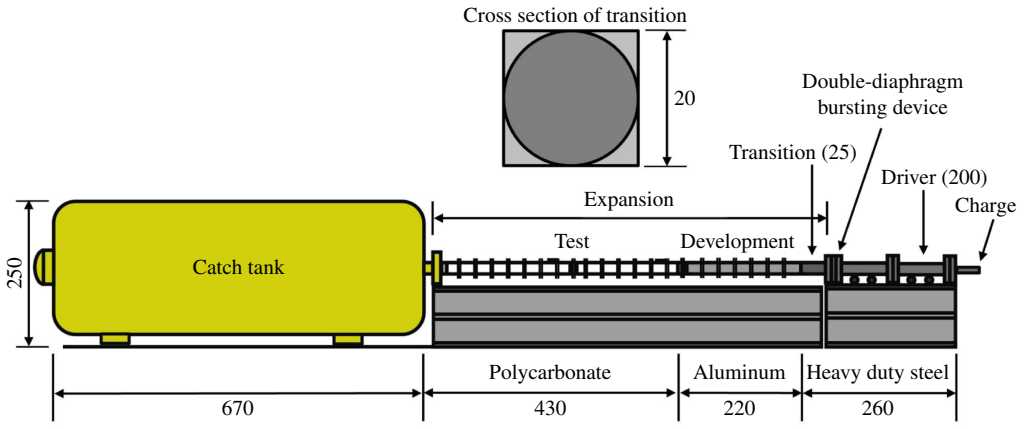

FIGURE 2. (Colour online) Schematic of the ASOS shock tube. All dimensions in centimetres.

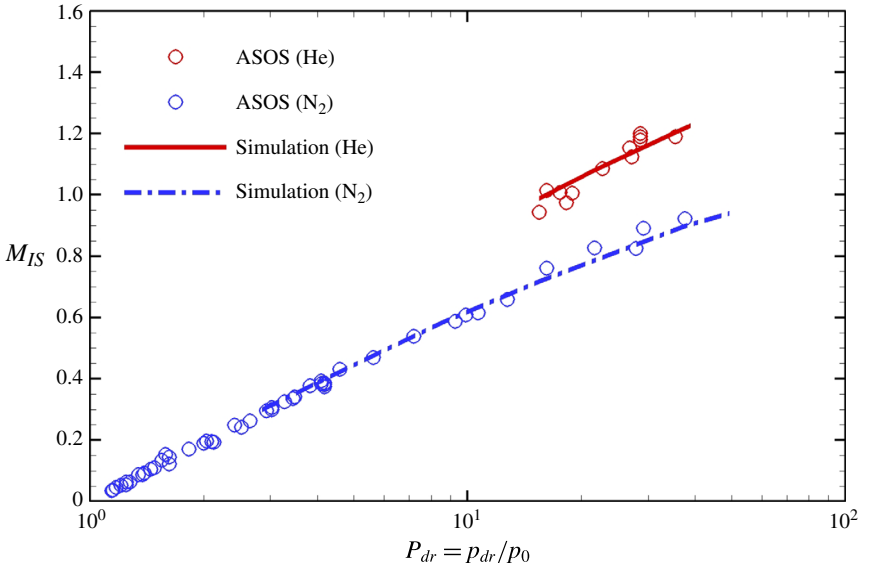

FIGURE 3. (Colour online) The experimentally accessible region in the ASOS facility. M_{IS} is the flow Mach number behind the incident shock, p_{dr} is the initial pressure in the driver, and p_0 is the initial pressure in the expansion section (1 atm). The flow conditions of the experimental points were obtained from the measured shock pressure ratios. Many runs from the operation of the shock tube are included along with those obtained in the present set. The lines are from numerical simulations of the whole-tube gas dynamics using the code of Chang & Liou (2007).

of the driver pressure with a maximum uncertainty of ± 2.5 ms. The operating range of the shock tube is illustrated in figure 3, which also demonstrates the theoretical support of the measured shock wave amplitudes. The scatter in data points is covered by accuracy of the pressure sensors (2 %) and gauge used to charge the driver

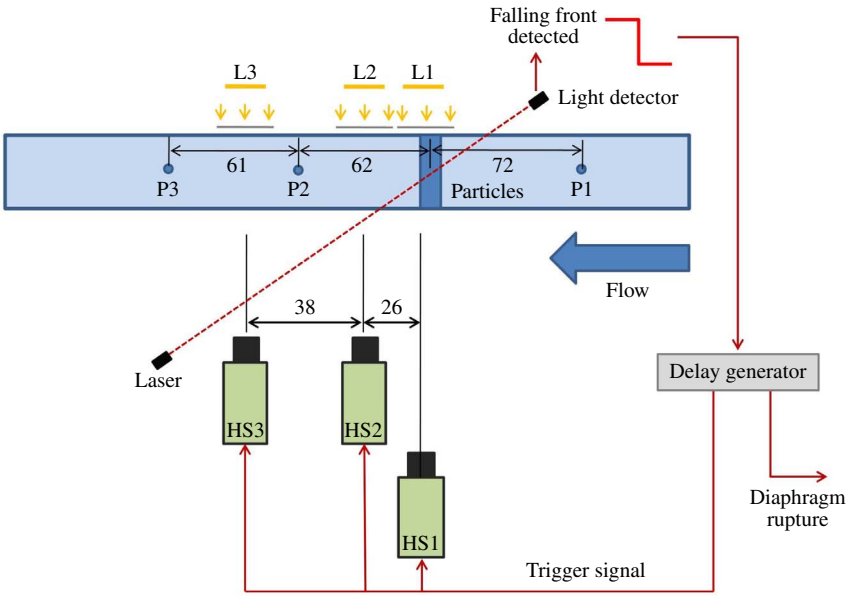

FIGURE 4. (Colour online) The instrumentation schema. All dimensions in centimetres. The high-speed video cameras are marked by HS1, HS2, HS3. Pressure transducer locations are marked by P1, P2, P3. Top view.

(1 %). Of course helium is more effective (than nitrogen) in creating stronger shocks, but it is quite expensive, so we choose to use it only when necessary by design considerations.

The instrumentation schema is illustrated in figure 4. For visualization we employ the shadowgraphic method with high-speed digital cameras from Vision Research. Camera HS1 is a Phantom V12, capable of 1 megapixel at up to 6.2 kHz, and HS2/HS3 are Phantom 7.1 cameras allowing 0.5 megapixel at up to 6.7 kHz. In this application we operate the cameras at 10 kHz, thus sacrificing about half of the pixel capability in favour of obtaining adequate time resolution at the high-end of the pressure ratios. Exposure times are limited by camera sensitivity to 5 μs, and with appropriate optics we obtain resolutions of ∼10 pixels per particle in a field of view of the full curtain at HS1. The lights for shadowgraphic imaging are provided by four white-light lamps (500T3/Q/CL 300 W). The pressure transducers are of the piezoelectric type, Kistler models 601A at position P1 and 211B3 at positions P2, and P3, with ranges 0–25 MPa and 0–3.4 MPa, respectively. The manufacturer calibrations were checked independently in our laboratory and found to be within the specified uncertainty (2 %). In a run, as the curtain enters the path to the light detector (ThorLabs PDA8A), a trigger signal is generated to sequence, with appropriate delays, diaphragm rupture and initiation of data acquisition by the cameras. The pressure transducer outputs are routed through signal amplifiers (Kistler 5010) to LeCroy Wave Surfer 424 digital oscilloscope, which triggers by incident shock front from P1 and records also the camera trigger for synchronization with the pressure transients.

In preliminary testing (Chang *et al.* 2011), we worked with particle curtains of low enough volume fraction to be considered dilute ($\alpha_d \sim 0.4\,\%$). These curtains were created by releasing particles through vibrating grids. In the present setting,

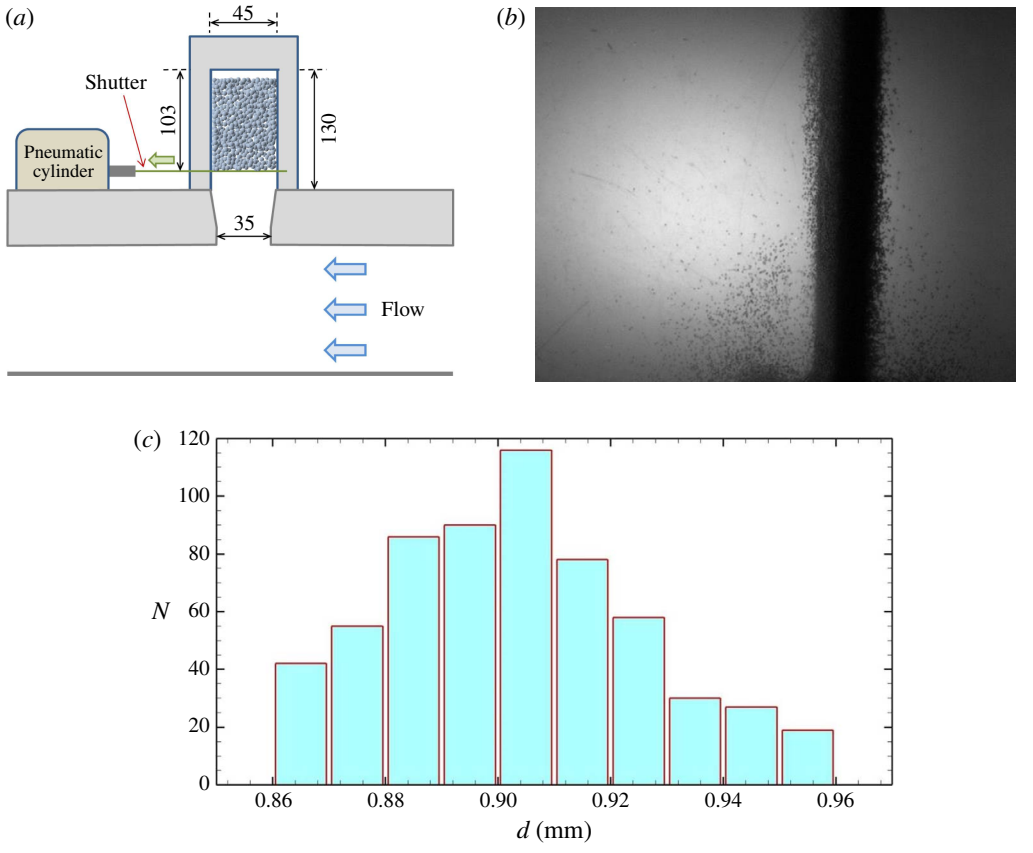

FIGURE 5. (Colour online) Schematic of the supply box and taper into the chute (*a*), visualization of a curtain at the time of shock impact (*b*) and size distribution of the particles utilized in the experiments (*c*). All dimensions in millimetres.

the particles are allowed to fall from a supply box, connected through a slight taper to a chute (figure 5*a*), so as to focus the particles into a curtain with well-defined boundaries (figure 5*b*). The release, by a quick-action shutter, is timed with driver-diaphragm rupture to yield shock impact coincident (±2.5 ms) with first formation of a full curtain. Based on extensive testing, we determined that this timing must involve a slight delay after the very first particles touched the channel floor, to exclude some non-uniformities associated with opening of the shutter. This created some 'floating' particles (bounced off the floor) before and after the curtain. Their effect is negligible. This also created a slight accumulation on the floor (a layer about 5 mm thick), which did eventually affect the interaction over the lowermost ∼10 % of the curtain, while also revealing some interesting particle-lifting phenomena that are of interest in their own right.

The glass particles were bought commercially (MO-SCI Specialty Products) and sieved carefully to isolate the particle-diameter range, $0.85 < d < 1.0$ mm, used in these experiments. The size distribution was determined by microscopic analysis of a random sample of 600 particles, yielding $0.86 < d < 0.96$ mm. The distribution is shown in figure 5. Sphericity was measured with the help of high-resolution visualizations of multiple, randomly sampled particles, and found to be accurate

to within 2 %. The ideal soda-lime glass density is $\rho_d = 2.5 \times 10^3$ kg m^{-3}. We determined the density independently by measuring the free volume of a certain mass of glass spheres packed inside a graduated cylinder. This gave 2.46×10^3 kg m^{-3}, which is 98.4 % of the ideal value, a finding supported by our microscopic examination that revealed no significant gas intrusions.

In addition to ensuring a reproducible, optically high-quality curtain, we also paid special attention to the characterization of the particle volume fractions in it. To this end, the particle-supply device was fitted to an outside construction that matched exactly the actual experimental channel. In this way the cloud could be approached freely, and videos could be made from all sides simultaneously, including the upper interface inside the particle-supply box (see figure 5). From the latter, we determined the mass flow rate (7.79 kg s^{-1} $\pm$ 3 %) history over the useful/complete emptying transient ($\sim$ 125/225 ms events), and this, under free-fall acceleration (which was in agreement with direct velocity measurements), could be translated to the volume fraction distribution. As a diverse method, we placed blackened-particle marks at regular intervals in the supply box, and by visualizing their relative distances at the time the main front touched the channel floor we could determine the volume fraction distribution as a function of height. The results of both of these quantifications are consistent as represented in figure 6. This figure also provides an overall measure of reproducibility and uncertainty.

The curtain fits exactly over the whole of the channel cross-sectional area as illustrated in figure 7. This figure also shows the nomenclature employed throughout. The test conditions were selected to span the attainable flow Mach numbers, which, as indicated in table 1, are used to identify individual runs. In this table, the flow Mach number is $M_{IS} \equiv u_{IS}/c_{IS}$, where ($u_{IS}$, c_{IS}) are (gas, sound) speeds behind the shock; the shock Mach number is $M_s \equiv u_{s,IS}/c_0$, where c_0 is the speed of sound in the air ahead of the shock (346 m s^{-1} in this case); P_{IS}/P_W are the incident/reflected shock pressures, the latter from a hypothetical rigid wall at the position of the curtain (the relevance of the latter is discussed at the beginning of § 3), both normalized by p_0; and $t^*_{ub} \equiv t_{ub}/\tau$, where t_{ub} is the duration of uniform blast (constant flow condition behind the shock) at the curtain position and τ is a characteristic time to be defined shortly. The time of uniform blast is limited by the reflected shock reflecting back to the curtain off the incident contact. The proximity of this contact with the incident shock wave increases with shock strength, and this results in diminishing t_{ub} as indicated in the table 1. The maximum Reynolds number (Re_{max}) is based on particle diameter and free-stream velocity behind the shock: it does not exist as such anywhere, but it may be useful as a basis for comparison between runs. It can be seen that the flow speeds in this set of runs vary from $\sim$100 to $\sim$700 m s^{-1}.

3. Experimental results

We have organized the presentation of results in two subsections covering respectively: pressure transients and 2D wave shapes (§ 3.1), and curtain displacements and cloud morphologies (§ 3.2). The cross-flow particle motion ('lifting') from the small amounts found on the channel floor is illustrated in appendix B.

Due to the very high density ratio, particle motion on the acoustic time at the particle scale is negligible, so the characteristic length is the initial curtain thickness (it is used to scale distances and displacements throughout), the actual value as found in the respective video is used in each case. In seeking the characteristic time, we recognize the importance of the pressure gradient across the curtain in the

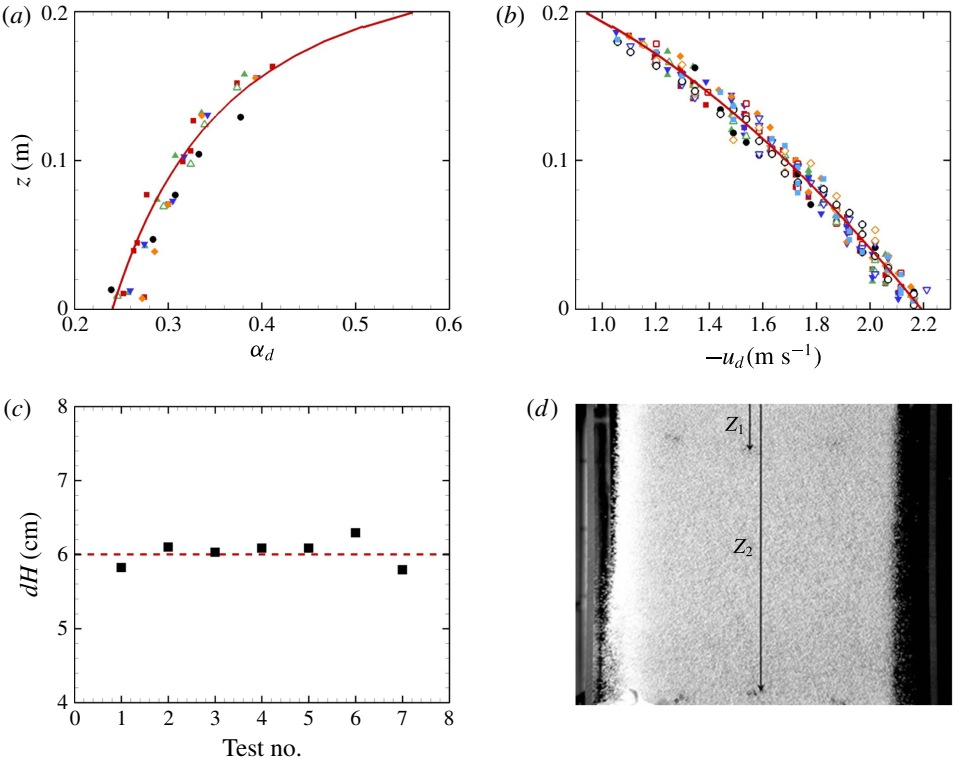

FIGURE 6. (Colour online) (*a*) The vertical volume fraction distribution in the ASOS curtain. The line is calculated from the mass flow rate and velocity measurements, shown in (*b*), and the data points are from direct measurements of volume expansion between particle markers in the supply load. The line in (*b*) is calculated assuming free-fall. (*c*) An overall measure of uncertainty in determination of volume fractions in the curtain; seven independent runs. The volume fraction distribution (*a*), was integrated to find the volume of particles between two extreme markers in the curtain (*d*), and this was compared with the actual volume known from the placement of these markers inside the supply box: both volumes converted to per unit area of the supply box; true value $dH = 6$ cm. All measurements taken at the time corresponding (± 2.5 ms) to shock impact in an actual test run. Notable is the large vertical gradient of volume fraction in the curtain; imposed by the free-fall condition, most of it is contained in the upper 20 % of the curtain's height.

momentum exchange process. Moreover, we anticipate, and subsequently verify, that, for the high-speed flows of concern here, the pressure reflection off the upstream face of the curtain would be quite similar to that off a rigid/impermeable wall (the p_W quantity introduced earlier). Thus, in the early, all-too-crucial portion of the transient the pressure gradient should be $(p_W - p_0)/l_0$, which together with the characteristic length, and mass (involving the density of the disperse phase), reveals (theory of dimensions) the characteristic time scale of the process as

$$\tau = l_0 \sqrt{\rho_d / p_0 (P_W - 1)}. \tag{3.1}$$

This $P_W \equiv p_W/p_0$ can be found from the positive root of the quadratic

$$\xi^2 - \left(2 + \tfrac{1}{2}\gamma(\gamma+1)M_{IS}^2\right)\xi + 1 - \tfrac{1}{2}\gamma(\gamma-1)M_{IS}^2 = 0, \tag{3.2}$$

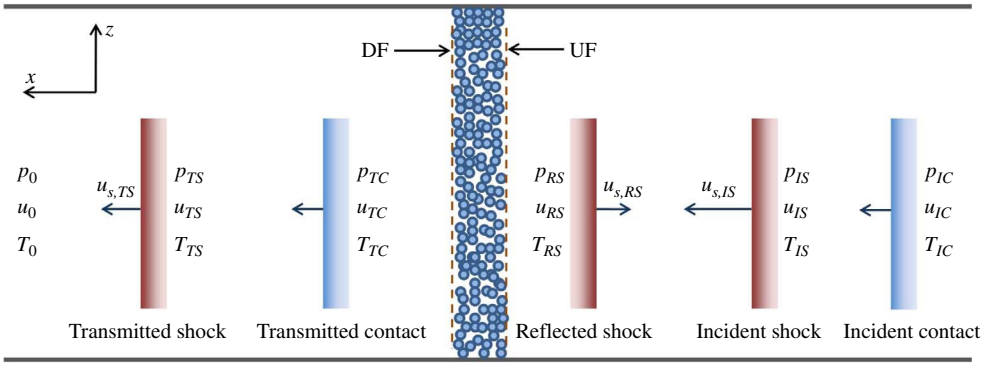

FIGURE 7. (Colour online) Illustration of the curtain geometry, pressure waves, contact waves, and related nomenclature. Here (p, u, T) is the gas flow state (pressure, velocity, temperature). The u_s are shock velocities. (UF, DF) designate the (upstream/downstream) fronts of the curtain.

Run no.	Driver gas	P_{IS}	M_s	P_W	τ (ms)	t^*_{ub}	Re_{max} ($\times 10^3$)	T_{IS} (K)	c_{IS} (m s^{-1})	l_0 (mm)
M0.29	N_2	1.52	1.20	2.28	3.11	4.26	7.7	337	368	29.6
M0.44	N_2	1.89	1.33	3.40	3.13	3.91	13	360	381	30.9
M0.57	N_2	2.34	1.46	4.96	2.23	3.30	19	387	394	28.2
M0.74	N_2	3.06	1.66	7.92	1.39	2.74	29	427	414	23.3
M0.92	N_2	4.19	1.93	13.40	1.23	2.30	42	487	443	27.5
M1.19	He	7.00	2.48	29.68	0.82	2.03	67	631	504	28.1
M1.23	He	7.60	2.58	33.40	0.63	1.86	71	661	516	22.7

TABLE 1. Summary of the test conditions investigated. All tests were conducted at standard atmospheric condition ($p_0 = 0.1$ MPa, $T_0 = 298.15$ K). A number of duplicate runs made to test reproducibility are not included in this table.

where $\xi = p_W/p_{IS}$, M_{IS} can be calculated from the applicable P_{IS}, and γ is the ratio of specific heats. Thus, we have the scaled quantities: $t^* \equiv t/\tau$, $X \equiv x/l_0$, and $L \equiv l/l_0$ where l is the curtain thickness at any time t after shock impact. For pressures, of principal importance are the incident and reflected shock pressure ratios, $P_{IS} \equiv p_{IS}/p_0$ and $P_{RS} \equiv p_{RS}/p_0$ respectively. The complete pressure transients we present in terms of $P \equiv p/p_0$. All displacements are relative to the initial UF of the curtain, and all times are referred to the instant of shock impact.

3.1. *Pressure transients and 2D wave shapes*

We use representative pressure transients (figure 8) to illustrate the main types of event in the curtain–shock interaction. These are: (i) reflection/transmission of shock waves following impact on the curtain; (ii) decay/surge of blast pressures upstream/downstream of the curtain as the curtain's permeability increases due to dispersal; (iii) cloud passage by the downstream pressure-measuring stations; and (iv) shaping and speeds of the reflected-shock and transmitted-contact waves, both generated upon shock impact as a result of rapid change in acoustic impedance. The following explanations are to be understood with the help of figures 8–10.

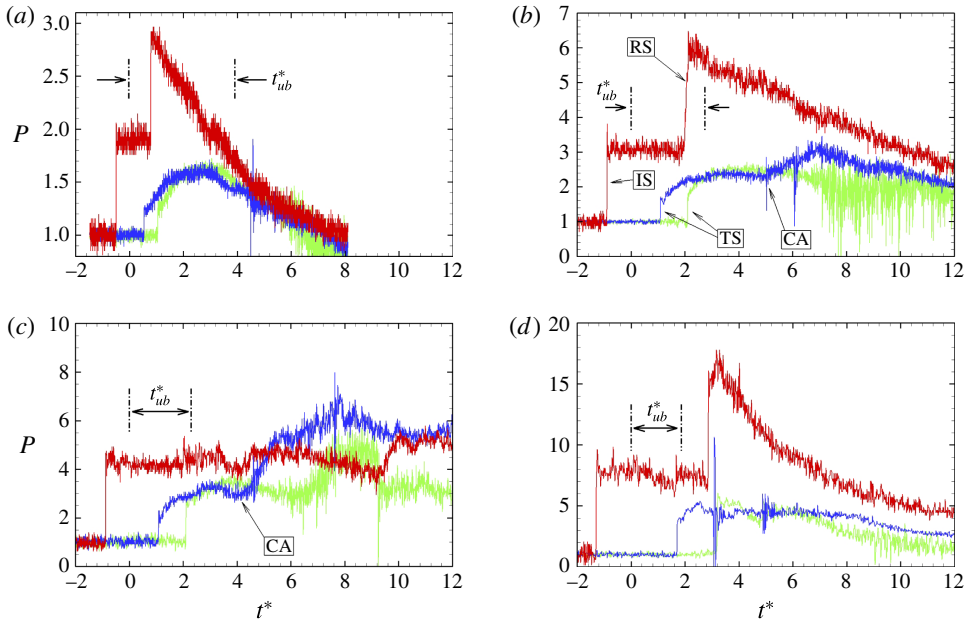

FIGURE 8. (Colour online) A sample of complete pressure transients: (*a*) M0.44, (*b*) M0.74, (*c*) M0.92, (*d*) M1.23. The marked 'uniform blast' period refers to the flow condition at the curtain as discussed in the text. 'CA' stands for cloud arrival. Red/blue/green refer to sensor positions P1, P2, P3, whose locations are shown in figure 4.

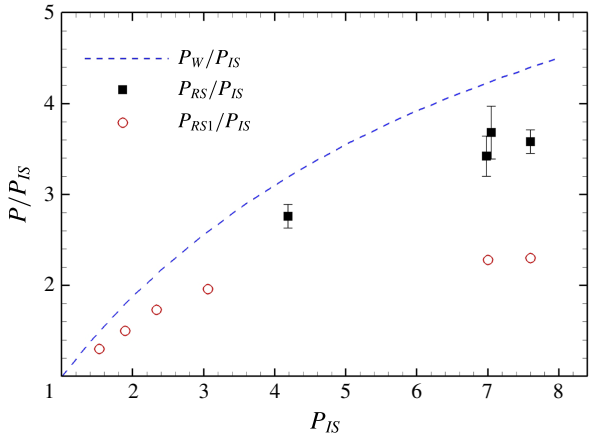

FIGURE 9. (Colour online) Variation of reflected shock pressure ratios with strength of the incident shock. Here P_{RS1} is reflected shock as measured on P1 and P_{RS} is reflected shock at the curtain position (see table 2 and associated text). The uncertainty bounds on P_{RS} correspond to the shock velocity values obtained by measuring translation from the left/right boundaries of the finite-thickness shock to the middle of the much sharpened shock on the next frame (see figure 10).

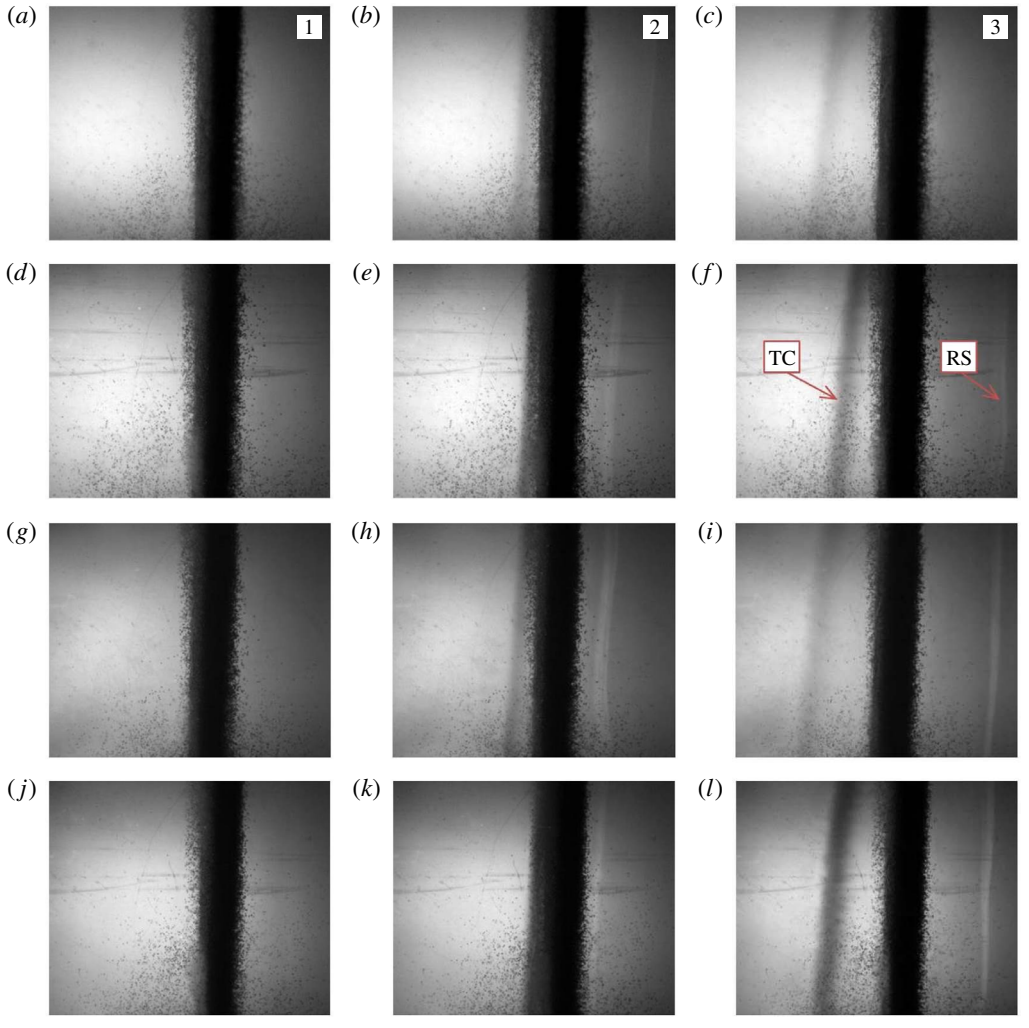

FIGURE 10. (Colour online) A sample visualization of reflected shock and transmitted contact waves in the early stages of shock–cloud interaction: (*a–c*) M0.74, $t = 0$; 0.3; 0.5 ms; (*d–f*) M0.92, $t = 0$; 0.2; 0.3 ms; (*g–i*) M1.19, $t = 0$; 0.2; 0.3 ms; (*j–l*) M1.23, $t = 0$; 0.1; 0.2 ms. All images show 15 cm from top to bottom. There is an absolute uncertainty in time (± 50 μs) due to the camera frame rate, but the relative uncertainty between successive frames, for computing speeds, is negligible.

(i) *Reflection/transmission of shock waves*. Arrival times at the upstream measuring station (P1), embody the competition between compressive transmission to the upstream and convection by the flow to the downstream. This competition is expressed by the net speed of the reflected wave: u_{RS}–u_{IC}. We can see that in scaled time the arrival of the reflected shock is delayed with increasing flow Mach number (figure 8), although in real time (see characteristic times in table 1) the delay is not quite as much. In the transonic run M0.92, the net speed becomes small enough that the reflected shock is not seen at P1 even well past the constant-blast time (figure 8*c*). At the supersonic condition, run M1.23, the incident contact follows closely the incident shock and gets to P1 before the

reflected shock; in this case, the high-amplitude reflected shock (see below) is able to reach P1, but only after it is partially quenched, as it has to pass through the incident contact (with very cold helium behind it) before reaching P1. As we demonstrate below, as a result of this quenching, the registered pressure at P1 (figure 8*d*) is much lower than the actual reflected pressure at the curtain position.

The amplitudes of reflected waves (figure 9) increase with increasing strength of the incident shock, in 'parallel' with what would be expected in a reflection from a solid wall. The approach is within 85–75 % as the P_{IS} varies from 1.5 to 3. For the supersonic (helium-driven) runs M1.19 and M1.23 the reflected shock is significantly quenched by the contact as noted above. Finally, in comparison with the reflected shock, the strength of transmitted waves is seen to be rather modest and increase rather slowly with flow Mach number (figure 8).

(ii) *Decay/surge of blast pressures*. As we will see in the next subsection, the curtains expand rapidly. The so-obtained increase in permeability is evidenced by the decay in the succession of reflected pressure waves and surge of transmitted waves as seen in figure 8. Note that in the scaled time of this figure these expansion processes and their effects on pressure responses both upstream and downstream of the curtain appear to be similar over a time frame of $t^* < 1.5$. In the next subsection, we will see that this is the time frame for the main (accelerated) expansion regime. These decay/surge transients provide a sensitive measure of how well curtain dispersal is reflected into the curtain permeability in numerical simulations of such events.

(iii) *Cloud passage by the pressure-measuring stations*. Run M0.74 shows clearly the cloud arrival at both positions, P2 and P3 (figure 8*b*). At P3, the cloud is more dispersed and this results to more violent oscillations of the pressure signal. At P2, we can see the whole event, as evidenced by the 'passing by' of the pressure gradient found within the cloud. We can see these same signatures, albeit more intense, at the higher Mach number run M0.92 (figure 8*c*), while at the still higher M1.23, by the time the cloud arrives at P2 and P3, it is significantly dispersed and sustains no pressure gradient. However the noise associated with cloud passage is quite visible. In scaled time, these (cloud-passage) events are reasonably coincident. In the next subsection we explain why this is so.

(iv) *Shaping and speed of the contact and reflected-shock waves*. The vertical volume fraction gradient, and associated acoustic impedance as well as permeability variations were directly visualized through the reflected shock and transmitted contact waves. A sample of such results is provided in figure 10. The reflected shock is stronger in the upper parts, and therefore it travels faster, while the contact permeates faster through the lower parts. The transmitted shocks are of much lower strength, rather elusive in that they transit through the field of view very rapidly, and not as interesting for purposes of a general discussion. However, they are crucial in providing ground-truth in assessing numerical simulations; these data are shown in figure 8.

The measured speeds of shocks and contacts as obtained from the images of figure 10 are summarized in table 2, which also shows the translation of these speeds to shock amplitudes. The method of estimating uncertainty is explained in the caption of figure 9. In run M1.19, the shock appeared in three frames, which allows us to understand the direction and roughly the magnitude of changes with time. In table 2 we see that the shock amplitude tends to decrease with time, while the contact speed tends to increase. Likely, they reflect changes of cloud

Run no.	P_{IS}	$u_{s,RS}$ (m s^{-1})	p_{RS} (bar)	p_W (bar)	$(u_{IS} - u_{s,RS})$ (m s^{-1})	u_{TC} (m s^{-1})
M0.92	4.19	−291.5	11.5	13.4	700.1	191.5
M1.19	7.01	−314.6	25.7	29.7	913.8	280.9
	7.01	−283.7	23.9	29.7	882.9	304.8
M1.23	7.60	−291.5	27.2	33.4	923.9	314.1

TABLE 2. Measured RS and TC wave speeds from the visualizations of figure 10. For run M1.19 the reflected shock appears in three consecutive frames (the third frame is not included in figure 10); the two entries correspond to the two velocity measurements between successive images. Transmitted contact velocities u_{TC} for runs (M0.57, M0.74) are (85, 136) m s^{-1}.

permeability with time. These results of relatively small, but clear variations with time provide important benchmarks for numerical simulations. In figure 9 we can see that the reflected shock at the curtain position is quite close (typically within 10–20 %) from the value resulting from reflection off a rigid wall.

3.2. *Curtain displacements and cloud morphologies*

The topological evolutions of the dispersing clouds are quite self-similar across all flow conditions: as illustrated in figure 11, only the rates of expansion vary with incident shock strength. Note that the UF front tilts, but only slightly, while the DF exhibits a differential expansion, from top to bottom by about 20 %. Superficially, this might suggest that the rate of expansion is favoured (in a quasi-1D view) by decreasing particle volume fraction, but this would be in conflict at the limit of dilute dispersions that yield no significant dynamic expansion. Rather, we expect that cloud permeability variations, as noted already, and associated cross-flow, pressure-rebalancing phenomena, would impose effectively higher/lower pressures at the bottom/top elevations of the upstream boundary of the cloud, thus biasing the accelerations (and expansions) in the manner seen in figure 11. As an interesting aside, we note the small waviness at the DF. It is limited, and oblique visualizations did not reveal anything else remarkable about it.

The UF/DF positions with time were quantified visually, for the mid-height elevation, by two experienced individuals working independently. At position HS1, at early times, the fronts are sharp (as in figure 11), and a front position was recognized, and marked, as the point where no light could be seen coming through the cloud (from Monte Carlo simulations we find that a 2 % volume fraction is sufficient to block all light). At later times, when the fronts become somewhat diffuse, and we can count particles, we mark fronts so that they leave 1 % of the volume on the outside; that is, on a horizontal slit 1 cm high, total ∼6000 particles, we leave 30 particles each on the outside of the two fronts. The so-obtained data are summarized in figure 12. Yet more revealing is a plot of curtain thickness against time squared (figure 13*a*): a constant acceleration period is observed, which in scaled time is seen to last for up to $t^* \sim 1.0$ (figure 13*b*). During this time the cloud expands with a constant scaled acceleration of ∼3, and after a rather quick transition, it expands with a constant scaled velocity of 3.5 (figure 14). Thus, we have in general the cloud-expansion laws:

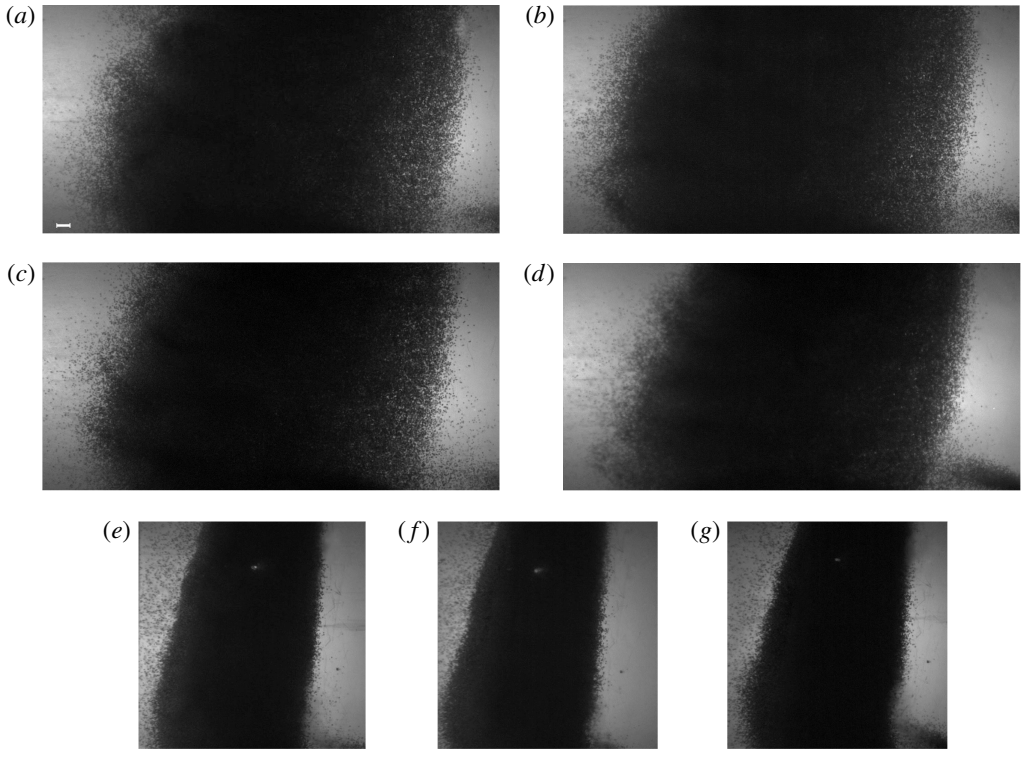

FIGURE 11. Cloud morphologies at position HS1, at near full coverage of the available field of view, which is smaller for the high-pressure runs due to additional structural supports needed for the channel walls: (*a–d*) runs M0.29, M0.44, M0.57, M0.74, at 10.0, 7.4, 5.6, 4.0 ms, respectively; (*e*,*f*) runs M0.92, M1.19, M1.23 at 1.6, 1.1, 1.0 ms, respectively. The white line on the first frame represents a length scale of 1 cm, which is the same for all frames (all images show 16 cm from top to bottom). The full videos can be found as supplemental material available at http://dx.doi.org/10.1017/jfm.2016.97.

$$\text{Constant acceleration regime (CAR):} \quad L \sim 1 + 1.5(t^*)^2 \quad (t^* < 1.4). \tag{3.3}$$

$$\text{Constant velocity regime (CVR):} \quad L \sim 2.5 + 3.5(t^* - 1) \quad (t^* > 1). \tag{3.4}$$

In the transition interval $1 < t^* < 1.4$ both cloud lengths and expansion velocities are nearly the same. The longer-term data obtained by reconstructing whole clouds from the video images in stations HS2 and HS3 (see appendix A) further support (3.4). They are not shown in figure 14 because the much larger scale required for them would diminish clarity in the important transition period. The method of assembling these composite clouds is described in appendix A, and it has been verified by comparison with a case that the whole cloud at HS2 happened to be captured in just one frame.

Returning to a couple of remarks we made in § 3.1, we can see the consistency, in scaled time, between cloud-expansion processes and pressure gradients sustained therein: 'in the scaled time of this (figure 8) these expansion processes and their effects on pressure responses both upstream and downstream of the curtain appear to be similar over a time frame of $t^* < 1.5$' and 'in scaled time these (cloud-passage) events are reasonably coincident'.

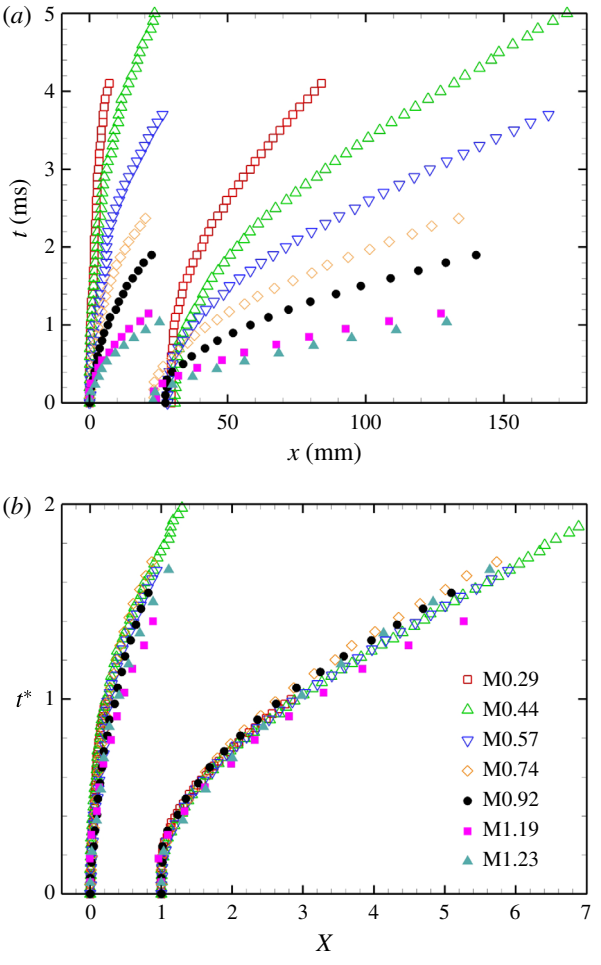

FIGURE 12. (Colour online) Trajectories of the upstream/downstream fronts (at curtain mid-height) in dimensional (*a*) and scaled (*b*) coordinates.

4. Discussion

From (3.3) we learn that the accelerated expansion process takes place in a rather short time, and while the cloud is still quite compact, capable of imposing a significant pressure gradient within. At the end of this process, $t^* \sim 1.4$, we have $L \sim 4$, that is a cloud expansion by a factor of four, which for the mid-height elevation translates to an (average) volume fraction of ∼7–8 %. Despite the significant changes in several processes that co-participate in this highly dynamic period, the net result is a remarkably constant acceleration in cloud expansion. The linear period that follows is markedly dependent upon the velocities attained at the end of this constant-acceleration regime, so the latter can be considered as dominating the entire dispersal event.

From the magnitude of the pressure gradients involved, and the scaling power of our characteristic time, we can expect the pressure gradient (or Archimedes) force to be important. The same is obviously true for the drag forces. As the cloud expands, the Archimedes force decreases, the gas-dynamic pressure increases, which

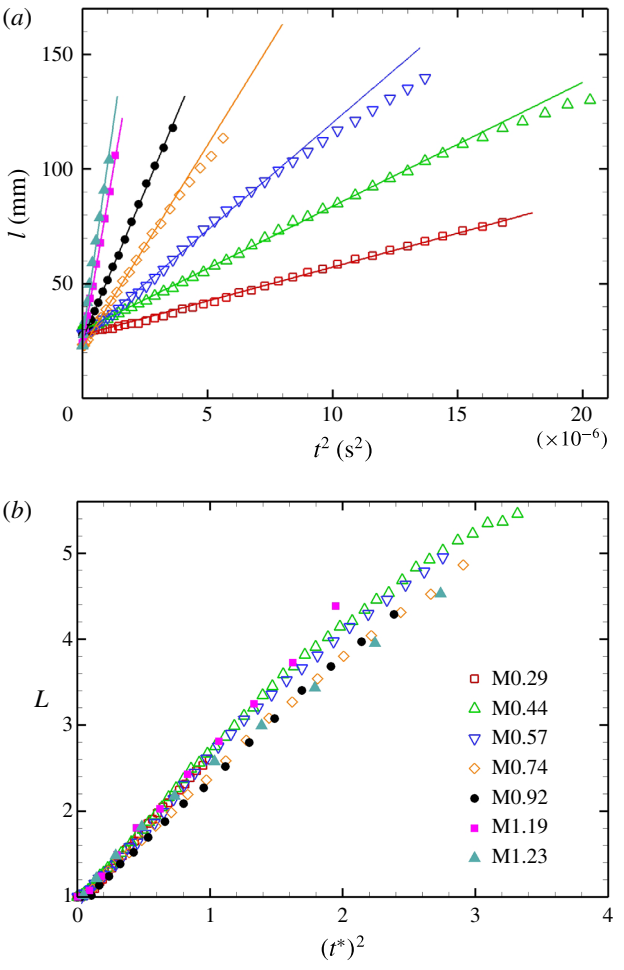

FIGURE 13. (Colour online) The constant-acceleration regime of cloud expansion, in dimensional (*a*) and scaled (*b*) coordinates.

contributes to an increased drag and at the same time the drag augmentation due to the collective effect of particles decreases. These interplays are present even at the same instant within the cloud due to non-uniformities in volume fraction and due to gas compressibility. Remarkably, all of these changes seem to just balance each other to produce a steady acceleration. Finding out the details of how this occurs has to await numerical simulations that provide consistent interpretations of pressure waves, contact waves and cloud trajectories, and we will address this in a separate paper.

Perhaps even more surprisingly, the cloud-expansion laws in (3.3) and (3.4) turn out to be applicable as well to the data of Wagner *et al.* (2012), notwithstanding great differences in experimental conditions. These include order-of-magnitude differences in particle size and curtain thickness, as summarized in table 3. A fuller relation of these experiments to ours can be found by comparing table 4 with table 1. Indeed, their data plotted on our time scale (figure 15) exhibit the two expected regimes, over exactly the same (scaled) time periods; albeit, because of the much shorter characteristic time (see table 4) the CAR contains only two or three data points

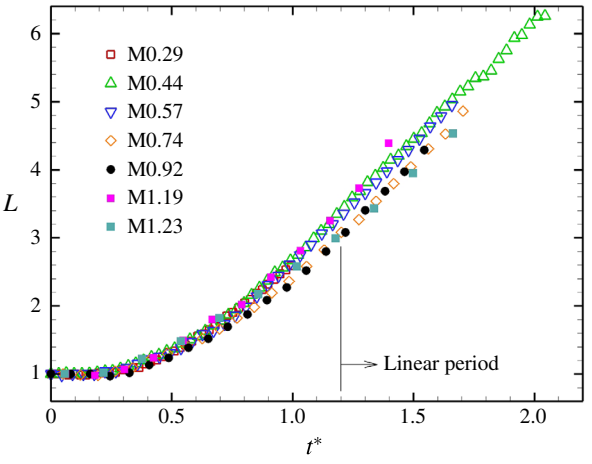

FIGURE 14. (Colour online) The linear-growth regime of cloud expansion.

	Particle diameter (μm)	Volume fraction	Curtain thickness (mm)
Wagner *et al.* (2012)	106–125	0.33–0.15	2
Present	860–960	0.58–0.24	30

TABLE 3. Summary of curtain characteristics in the Wagner *et al.* (2012) tests in comparison with ours.

Run no.	Driver gas	P_{IS}	M_s	P_W	τ (μs)	Re_{max} ($\times 10^3$)	T_{IS} (K)	c_{IS} (m s^{-1})
M0.74	N_2	3.05	1.66	7.89	120	3.6	426	414
M0.97	N_2	4.6	2.02	15.54	82	5.8	508	452

TABLE 4. Key data for comparison between the present set of experiments (table 2) and those of Wagner *et al.* (2012).

for each run, and it could have been missed, if not knowing to look for it. Ling *et al.* (2012) scaled the Wagner *et al.* (2012) data by acoustic, and flow transit times through the curtain. They concluded the later was satisfactory. Our own data scaled in these two ways are shown in figure 16. The former exhibits a CAR-like behaviour but fails to scale the data. The latter produces weak scaling and fails to exhibit the CAR.

5. Conclusions

We draw the following conclusions.

(i) Following impact by shock waves, dense particle clouds expand rapidly. The entire expansion process consists of two regimes. In the first, the rate of expansion maintains a remarkably constant acceleration, hence the constant-acceleration regime. In the second, the rate of expansion itself remains remarkably constant, hence the constant-velocity regime. The transition period

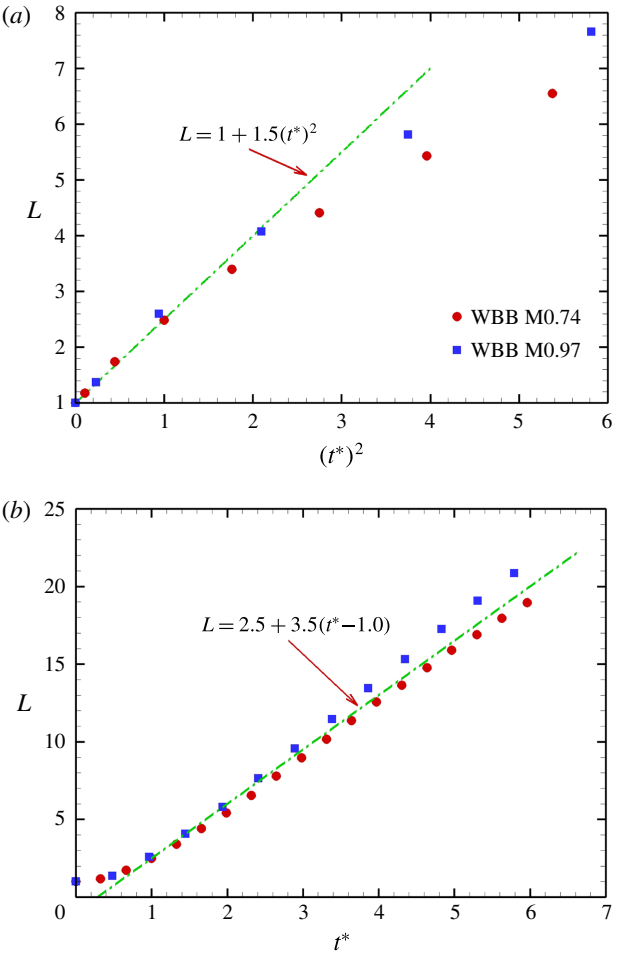

FIGURE 15. (Colour online) The cloud expansion data of Wagner *et al.* (2012), via Ling *et al.* (2012), recast in our scaled coordinates. (*a*) Constant-acceleration regime and (*b*) constant-velocity regime.

between the two regimes is rather brief and it seems to relate to the cloud becoming dilute (volume fractions about 4–8 %) and unable to sustain significant pressure gradients. This behaviour is similar across all flow conditions from subsonic to supersonic, and encompasses experiments with particle sizes and curtain thicknesses differing by an order of magnitude.

(ii) Incident shock reflection from the upstream front of the cloud involves the same nonlinearities due to compressibility as reflections from a solid wall, but magnitudes are somewhat smaller due to finite cloud permeability. The magnitude of reflected shock, curtain thickness, and disperse-phase density provide the characteristic time ($\tau = l_0\sqrt{\rho_d/p_0(P_W - 1)}$) for this expansion process: the resulting scaling reveals the two regimes of expansion, unifies the behaviour within each one of them and leads to simple scaling laws for cloud dimensions $L \sim 1 + 1.5(t^*)^2$ and $L \sim 2.5 + 3.5(t^* - 1)$ for CAR and CVR, respectively. The demarcation is over a transitional interval $1 < t^* < 1.4$ where either law is accurate enough.

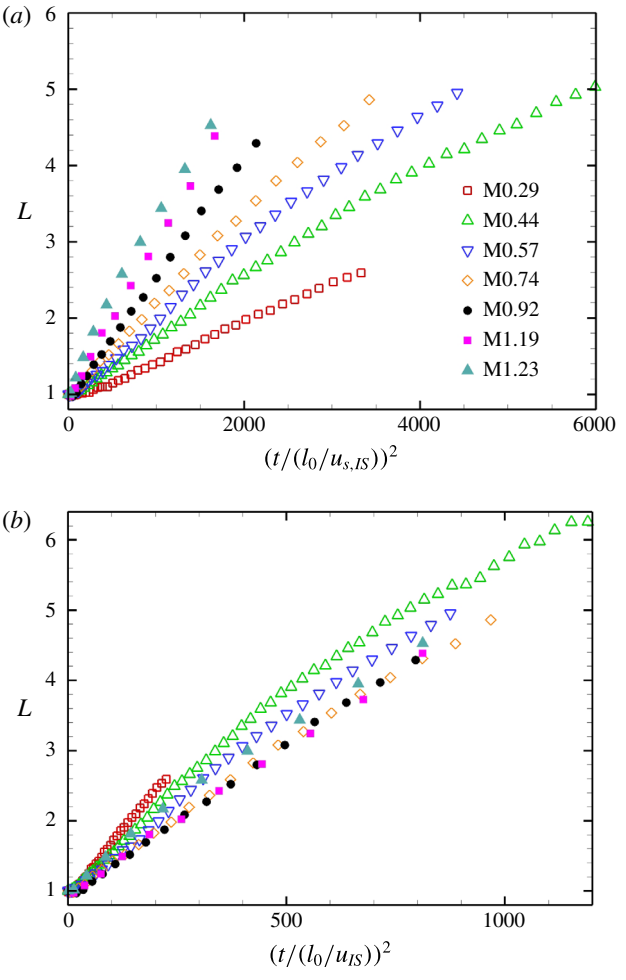

FIGURE 16. (Colour online) Our cloud-expansion data under the scaling of Ling *et al.* (2012).

(iii) In dimensional terms, the magnitude of the acceleration (in expansion rate) is proportional to the amplitude of the reflected shock, which is close to that reflecting from a solid wall, and inversely proportional to the cloud inertia, as expressed by the product (curtain thickness) × (particle density). Notably, within the range of the two sets of experiments considered here, the particle size does not enter.

(iv) The experimental data of Wagner *et al.* (2012), even though taken at significantly different conditions (notably an order smaller particles), by employing significantly different methods, exhibit quantitatively similar behaviours.

Acknowledgements

The ASOS facility and related modelling/computational program were sponsored by the Defense Threat Reduction Agency (DTRA).

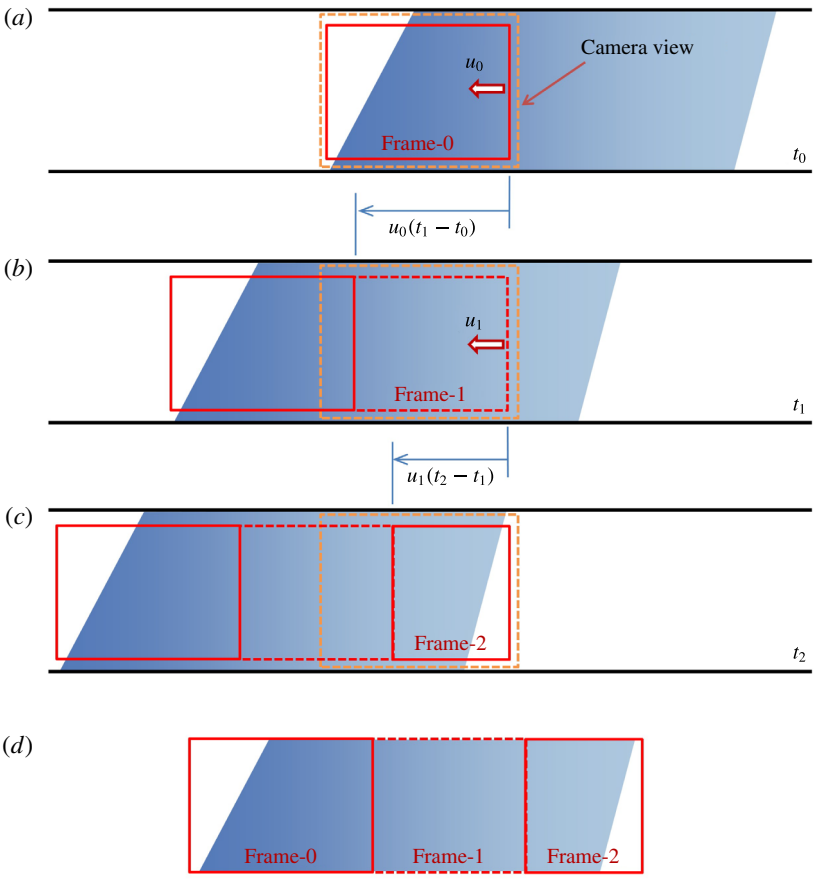

FIGURE 17. (Colour online) The cloud-assembly methodology for videos taken at positions HS2 and HS3. At time t_0 we find the average particle velocity u_0 at the right boundary of frame 0. At time t_1, this boundary is displaced by $u_0(t_1 - t_0)$, and this then is the left boundary of frame 1. Continuing this process until the cloud is assembled, as shown in (*d*) for this three-frame cloud.

Supplementary movies

Supplementary movies are available at http://dx.doi.org/10.1017/jfm.2016.97.

Appendix A. Long-term cloud morphologies and speeds

We were able to reconstruct the fully dispersed clouds in the long-term by assembling frames in the manner illustrated in figure 17. The results for positions HS2 and HS3 are summarized in figures 18 and 19 and table 5, respectively. One can see that the cloud lengths at these rather dilute states are consistent with the constant-velocity law (3.4).

Appendix B. The particle-lifting phenomenon

The initial condition for the 'puddle' of particles on the channel floor was estimated by assuming a near-close packing, and a near-uniform depth. The volume of such

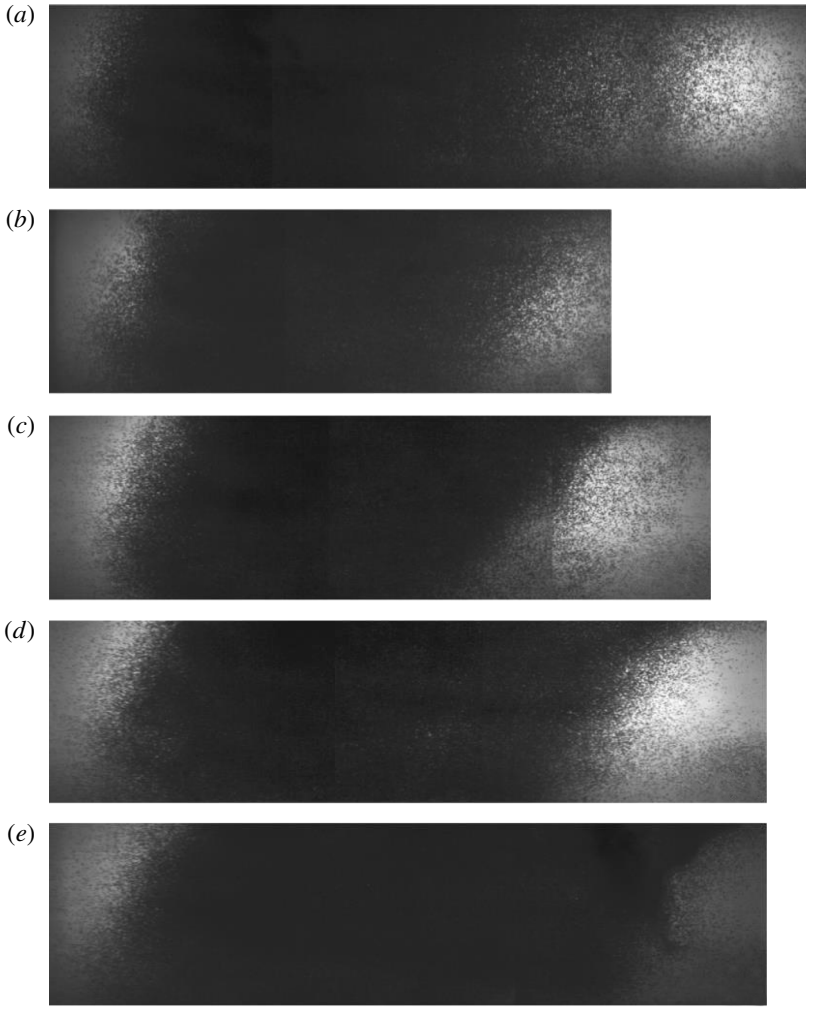

FIGURE 18. Assembled clouds at position HS2. (*a–e*) Runs M0.44, M0.74, M0.92, M1.19 and M1.23. All images measure 15 cm from top to bottom.

a puddle is known from the flow rate into the curtain and the time delay between the front contacting the floor and shock impact: it is 135 cm^3 and corresponds to $\sim$10 % of the curtain volume. In this time interval, these extra particles had spread over 15 cm on the channel's length-wise direction, covering a floor area of 300 cm^2. Thus, we estimate an average puddle depth of $\sim$5 mm.

The lifting–jetting phenomenon observed was similar across all runs; as was the case for curtain expansion, it varies only in intensity. A typical illustration is provided in figure 20. For space efficiency in this figure, the framing of each image varies somewhat in the axial direction: the exact coordinates relative to a fixed point on the channel are shown on the frames that contain the velocity vectors.

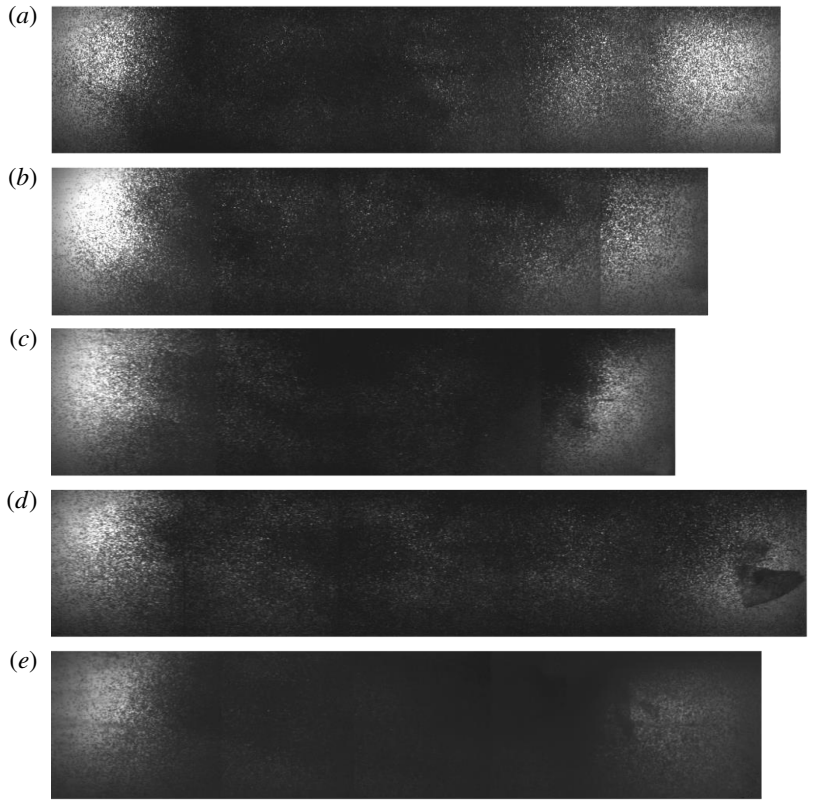

FIGURE 19. Assembled clouds at position HS3. (*a–e*) Runs M0.44, M0.74, M0.92, M1.19 and M1.23. All images measure 15 cm from top to bottom.

Run no.	Position	t^*	L (measured)	L (from (3.4))	Cloud speed (m s^{-1})		
					u_{DF}	u_M	u_{UF}
M0.44	HS2	3.8	16.2	12.4	73	59	44
	HS3	5.8	21.0	19.1	81	60	42
M0.74	HS2	4.9	15.9	16.1	130	120	110
	HS3	6.5	22.9	21.7	155	140	125
M0.92	HS2	3.8	13.3	12.1	160	145	130
	HS3	5.1	18.2	17.0	210	200	190
M1.19	HS2	3.9	15.1†	12.6	220	190	170
	HS3	6.0	23.1	19.8	260	230	195
M1.23	HS2	4.6	19.8†	15.2	235	200	175
	HS3	6.9	23.6	23.1	290	240	220

TABLE 5. Summary of results from videos at HS2 and HS3. The u_M is the speed at the approximate cloud mid-length.

†Incident contact has caught up with the cloud.

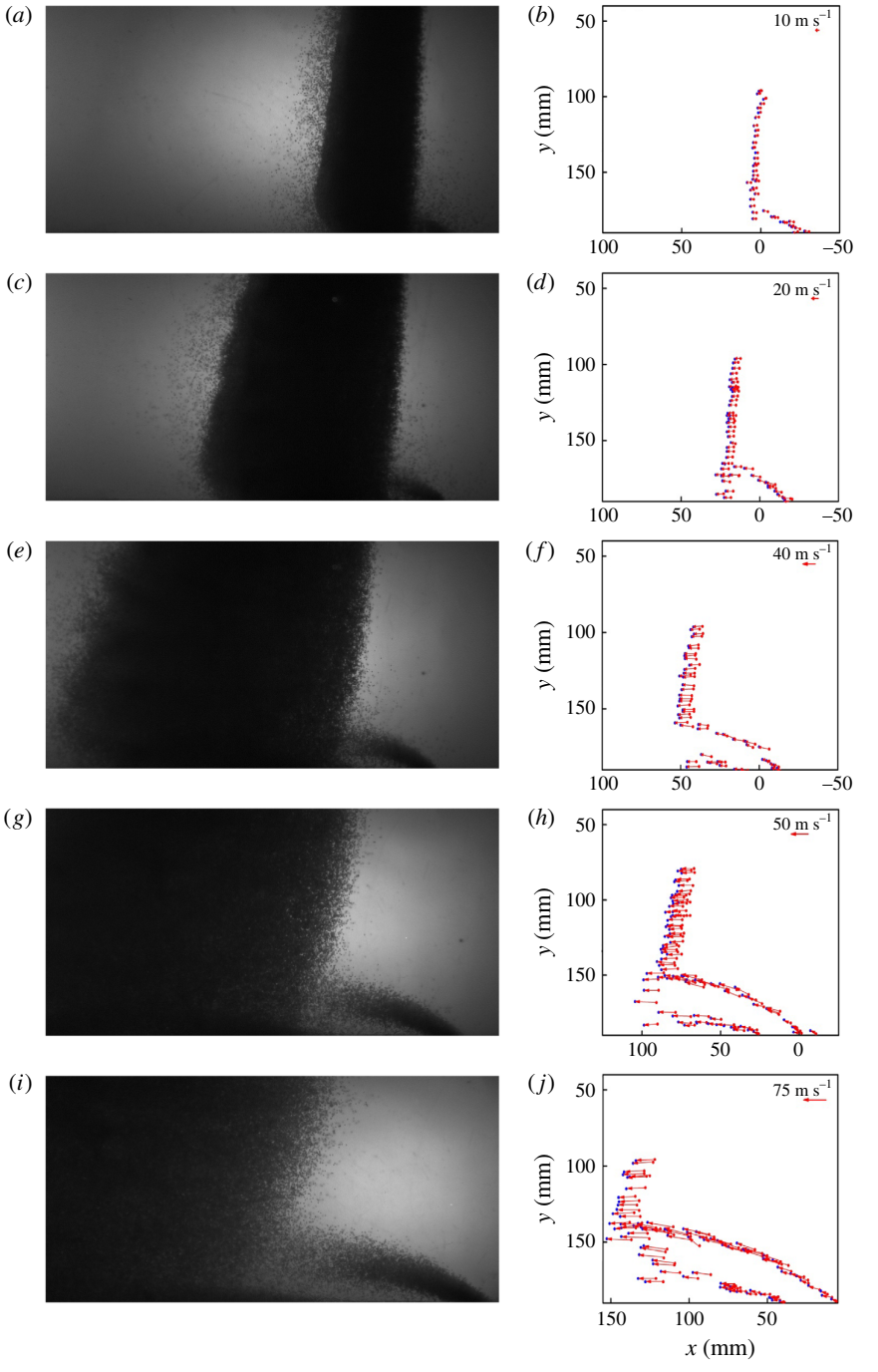

FIGURE 20. (Colour online) Illustration of the lifting-jetting phenomenon (run M0.74); frames are shown at 1 ms intervals starting at 1.5 ms. Dots show initial (red) and final (blue) positions of particles over a time increment of $\Delta t = 200$ μs. Images and plots are in the same scale; the right edge of each frame has the same coordinates as in the corresponding plot.

REFERENCES

BABARSKY, R. & THEOFANOUS, T. G. 2010 An assessment of the state-of-the-art on aerodynamic/explosive dissemination of chemical agents with perspectives for future work *Tech. Rep.* WF-67774. National Ground Intelligence Center, US Army.

CHANG, C.-H., DENG, X. & THEOFANOUS, T. G. 2013 Direct numerical simulation of interfacial instabilities: a consistent, conservative, all-speed, sharp-interface method. *J. Comput. Phys.* **242**, 946–990.

CHANG, C.-H. & LIOU, M.-S. 2007 A robust and accurate approach to computing compressible multiphase flow: stratified flow model and AUSM^{+}-up scheme. *J. Comput. Phys.* **225**, 840–873.

CHANG, C.-H., SUSHCHIKH, S., MITKIN, V. & THEOFANOUS, T. G. 2011 Shock-induced fluidization. In *20th AIAA Computational Fluid Dynamics Conference, Honolulu, Hawaii*.

LING, Y., WAGNER, J. L., BERESH, S. J., KEARNEY, S. P. & BALACHANDAR, S. 2012 Interaction of a planar shock wave with a dense particle curtain: modeling and experiments. *Phys. Fluids* **24**, 113301.

REGELE, J. D., RABINOVITCH, J., COLONIUS, T. & BLANQUART, G. 2014 Unsteady effects in dense, high speed, particle laden flows. *Intl J. Multiphase Flow* **61**, 1–13.

SUBRAMANIAM, S. 2013 Lagrangiane–Eulerian methods for multiphase flows. *Prog. Energy Combust. Sci.* **39**, 215–245.

THEOFANOUS, T. G. 2011 Aerobreakup of Newtonian and viscoelastic liquids. *Annu. Rev. Fluid Mech.* **43**, 661–690.

THEOFANOUS, T. G., MITKIN, V. V. & NG, C. L. 2013 The physics of aerobreakup. iii: viscoelastic liquids. *Phys. Fluids* **25**, 032101.

THEOFANOUS, T. G., MITKIN, V. V., NG, C. L., CHANG, C.-H., DENG, X. & SUSHCHIKH, S. 2012 The physics of aerobreakup. ii: viscous liquids. *Phys. Fluids* **24**, 022104.

THEOFANOUS, T. G., NOURGALIEV, R. R., LI, G. J. & DINH, T. N. 2006 Compressible multi-hydrodynamics (cmh): breakup, mixing, and dispersal, of liquids/solids in high speed flows. In *Proceedings of an IUTAM Symposium on Computational Approaches to Disperse Multiphase Flow* (ed. S. Balachandar & A. Prosperetti), pp. 353–369. Springer.

WAGNER, J. L., BERESH, S. J., KEARNEY, S. P., TROTT, W. M., CASTANEDA, J. N., PRUETT, B. O. & BAER, M. R. 2012 A multiphase shock tube for shock wave interactions with dense particle fields. *Exp. Fluids* **52**, 1507–1517.